Monthly Notices
of the
ROYAL ASTRONOMICAL SOCIETY

MNRAS **509,** 5197–5208 (2022)
Advance Access publication 2021 November 23
https://doi.org/10.1093/mnras/stab3359

The updated BASTI stellar evolution models and isochrones – III. White dwarfs

Maurizio Salaris,[1,2]★ Santi Cassisi,[2,3] Adriano Pietrinferni[2] and Sebastian Hidalgo[4,5]

[1] *Astrophysics Research Institute, Liverpool John Moores University, 146 Brownlow Hill, Liverpool L3 5RF, UK*
[2] *INAF – Osservatorio Astronomico di Abruzzo, Via M. Maggini, s/n, I-64100 Teramo, Italy*
[3] *INFN – Sezione di Pisa, Largo Pontecorvo 3, I-56127 Pisa, Italy*
[4] *Instituto de Astrofisica de Canarias, Via Lactea s/n, E-38205 La Laguna, Tenerife, Spain*
[5] *Department of Astrophysics, University of La Laguna, Via Lactea s/n, E-38200 La Laguna, Tenerife, Spain*

Accepted 2021 November 17. Received 2021 November 5; in original form 2021 September 22

ABSTRACT

We present new cooling models for carbon–oxygen white dwarfs (WDs) with both H- and He-atmospheres, covering the whole relevant mass range, to extend our updated BASTI (a Bag of Stellar Tracks and Isochrones) stellar evolution archive. They have been computed using core chemical stratifications obtained from new progenitor calculations, adopting a semi-empirical initial–final mass relation. The physics inputs have been updated compared to our previous BASTI calculations: ^{22}Ne diffusion in the core is now included, together with an updated CO phase diagram, and updated electron conduction opacities. We have calculated models with various different neon abundances in the core, suitable to study WDs in populations with metallicities ranging from supersolar to metal poor, and have performed various tests/comparisons of the chemical stratification and cooling times of our models. Two complete sets of calculations are provided, for two different choices of the electron conduction opacities, to reflect the current uncertainty in the evaluation of the electron thermal conductivity in the transition regime between moderate and strong degeneracy, crucial for the H- and He-envelopes. We have also made a first, preliminary estimate of the effect – that turns out to be generally small – of Fe sedimentation on the cooling times of WD models, following recent calculations of the phase diagrams of carbon–oxygen-iron mixtures. We make publicly available the evolutionary tracks from both sets of calculations, including cooling times and magnitudes in the Johnson-Cousins, Sloan, Pan-STARSS, *GALEX*, Gaia-DR2, Gaia-eDR3, HST-ACS, HST-WFC3, and *JWST* photometric systems.

Key words: stars: evolution – stars: interiors – white dwarfs.

1 INTRODUCTION

According to theory, white dwarfs (WDs) are the most common final stage of the evolution of single stars. Indeed, all single stars with initial mass up to ~9–10 $M_{\odot}$ are predicted to end up as either He-core (for initial masses below ~0.5 $\mathrm{M}_{\odot}$), CO-core (initial masses between ~0.5 and ~6–7 $\mathrm{M}_{\odot}$), or ONe-core (initial masses between 6–7 and 9–10 $\mathrm{M}_{\odot}$) WDs, and due to the current age of the universe and the shape of the stellar initial mass function, the overwhelming majority of WDs produced so far by single star evolution are predicted to have a CO core.

In the last 25 yr, thanks to steady advances in both observations and theory, models of CO-core WDs have been used extensively in conjuction with photometric, spectroscopic, and asteroseismic data, to determine the ages of field WDs (e.g. Winget et al. 1987; Oswalt et al. 1996; Torres & García-Berro 2016; Kilic et al. 2017; Tononi et al. 2019) for constraining the star formation history of the Milky Way, the ages of WDs in open clusters (e.g. Richer et al. 1998; von Hippel 2005; Bedin et al. 2008, 2010, 2015; Bellini et al. 2010; García-Berro et al. 2010) and globular clusters (e.g. Hansen et al. 2004, 2007; Bedin et al. 2009, 2019; Winget et al. 2009; Goldsbury et al. 2012), and even as probes to investigate open questions in theoretical physics (e.g. Freese 1984; Isern, Hernanz & Garcia-Berro 1992; Garcia-Berro et al. 1995; Córsico et al. 2001; Benvenuto, García-Berro & Isern 2004; Winget et al. 2004; Bertone & Fairbairn 2008; García-Berro et al. 2011; Isern et al. 2018)

As part of an ongoing new release of the BASTI (a Bag of Stellar Tracks and Isochrones) stellar model library (Hidalgo et al. 2018; Pietrinferni et al. 2021), and given the important role played by evolutionary WD models to address a range of major astrophysics and physics questions, we present here new sets of CO-core WD model computations, that update the Salaris et al. (2010) calculations – hereafter S10 – part of the previous BASTI release, taking advantage of recent improvements in a number of stellar physics inputs. In these new calculations, that cover the whole relevant mass range, we have included the diffusion of ^{22}Ne in the liquid phase, which was not accounted for by S10, we have updated the electron conduction opacities, the phase diagram for CO compositions, and also the CO stratification in the cores of the models, as described in the next sections.

Following the recent analysis by Cassisi et al. (2021), we present calculations for two different choices of the electron conduction opacities, and we also provide a preliminary estimate of the effect

---

★ E-mail: M.Salaris@ljmu.ac.uk

Published by Oxford University Press on behalf of Royal Astronomical Society

on the model cooling times of iron sedimentation in the CO cores, based on the very recent study by Caplan et al. (2021) of the phase diagram of carbon, oxygen, and iron ternary mixtures. We make publicly available at the official BASTI website[1] the evolutionary tracks (cooling tracks) in the Hertzsprung–Russell diagram, including cooling times and magnitudes in several photometric filters, obtained for all WD masses and chemical stratifications presented here.

The plan of the paper is as follows. Section 2 describes the parameter space covered by our WD calculations, the adopted physics inputs and initial chemical abundance profiles, and the effect of the ^{22}Ne diffusion on both the chemical stratification and cooling times of the models. The following Section 3 presents numerical tests to quantify the effect of progenitor metallicity and the adopted relation between progenitor mass and final WD mass, on chemical profiles and cooling times. We also discuss how the cooling times are affected by considering the idealized, sharp chemical transitions between the CO core and the pure-He/H envelopes adopted in our models (and other models in the literature), and by neglecting the small fraction of heavy elements and atomic diffusion in the envelopes during the WD evolution. Section 4 compares the cooling times obtained with the two choices for the conductive opacities, while Section 5 presents a first preliminary estimate of the effect of iron sedimentation of our model cooling times. Section 6 compares cooling times and radii of our new calculations with models from the literature and is followed by a brief summary of our results which brings the paper to a close.

2 MODELS

We have calculated CO-core WD cooling models with pure-H (representative of H-atmosphere WDs) and pure He (representative of He-atmosphere WDs) envelopes, with masses $M_{\rm WD}$ equal to 0.54, 0.61, 0.68, 0.77, 0.87, 1.0, and 1.1 $M_{\odot}$, respectively. These masses are in common with our previous S10 calculations, apart from the highest value.

All computations include the important processes of diffusion of ^{22}Ne in the liquid phase of the CO-cores (see Bravo et al. 1992; Bildsten & Hall 2001; Deloye & Bildsten 2002; García-Berro et al. 2008; Althaus et al. 2010), latent heat release, and phase separation upon crystallization (see e.g. Stevenson 1980; Mochkovitch 1983; Garcia-Berro et al. 1988), which provide sizable contributions to the energy budget of the models.

As in our previous sets of calculations (Salaris et al. 2000 and S10), for each mass an initial model has been converged at $\log(L/L_{\odot}) \sim 1.0-1.5$, by considering a reference CO-core chemical stratification and a reference thickness and chemical composition of the envelope layers, described in Section 2.2.

For each mass and core chemical stratification, we have computed models for two different choices of the electron conduction opacities – from Cassisi et al. (2007) and Blouin et al. (2020), respectively – as described in Section 2.1. Figs 1 and 2 display, as an example, the radius of our grid of H-atmosphere and He-atmosphere models calculated with Cassisi et al. (2007) opacities as a function of the effective temperature $T_{\rm eff}$, and the resulting cooling tracks in selected colour magnitude diagrams (CMDs). We can easily notice in three of the displayed CMDs of H-atmosphere models the turn to the blue of the colours at faint magnitudes (more pronounced in infrared CMDs, like the HST-WFC3 ($F115W$, $F200W$) diagram) caused by the H_2 collision induced absorption in the atmospheres (see e.g. Hansen 1998; Saumon & Jacobson 1999). Mass–radius relations and CMDs for all models calculated with Blouin et al. (2020) opacities are identical to those displayed in these figures.

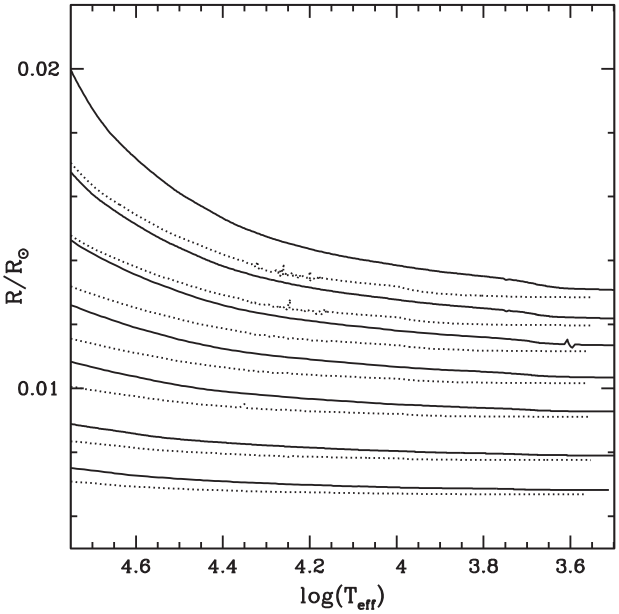

Figure 1. Radius of our grid of H-atmosphere (solid lines) and He-atmosphere (dotted lines) models calculated with Cassisi et al. (2007) electron conduction opacities, as a function of the models' $T_{\rm eff}$ (at fixed $T_{\rm eff}$ larger radii correspond to less massive models).

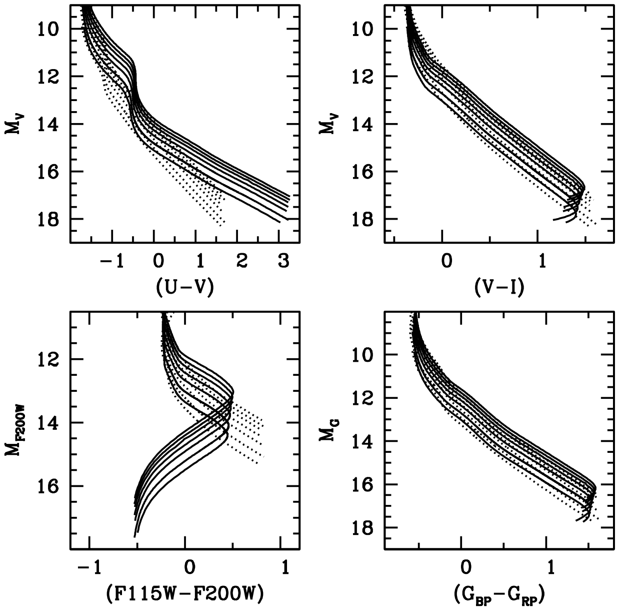

Figure 2. Selected CMDs of the models in Fig. 1 (solid lines for H-atmosphere models, dotted lines for He-atmosphere models) in Johnson-Cousins (upper panels), HST-WFC3 (bottom left-hand panel), and Gaia-eDR3 (bottom right-hand panel) filters.

---

[1] http://basti-iac.oa-abruzzo.inaf.it

2.1 Physics inputs

The WD evolution code employed for our calculations is the same described in Salaris et al. (2000) and S10. We briefly summarize here the main physics inputs and what has changed compared to S10.

The equation of state (EOS) for the H and He layers is from Saumon, Chabrier & van Horn (1995), supplemented in the liquid phase by calculations following Segretain et al. (1994) formalism; for the CO cores, we adopted Segretain et al. (1994) calculations in the solid and liquid phase and Straniero (1988) EOS for the gas phase. We have made some test calculations employing for the H and He layers the recent EOS published by Chabrier, Mazevet & Soubiran (2019), an update of the Saumon et al. (1995) one. We have found negligible differences in the structure and cooling times of the models, compared to computations with the Saumon et al. (1995) EOS.

Phase separation upon crystallization of the CO mixture is included employing the new phase diagram by Blouin & Daligault (2021), and the energy contribution due to phase separation is calculated following Isern et al. (2000).

The diffusion of ^{22}Ne (hereafter Ne) in the liquid layers of the CO cores is included following García-Berro et al. (2008) and Althaus et al. (2010). Neon is considered to diffuse as a trace element in a one-component plasma background – see equations (19) and (20) in García-Berro et al. (2008) – made of a fictitious element with mean atomic weight and charge calculated by averaging over the local number fractions of C and O. The Ne diffusion coefficients come from the most recent results by Hughto et al. (2010), and the contribution of this process to the energy budget has been calculated following García-Berro et al. (2008). We have not included phase separation of Ne in the core in the solid phase, a process whose occurrence is under debate. It is found to be efficient in WD cores by Blouin, Daligault & Saumon (2021) calculations, while Caplan, Horowitz & Cumming (2020) results show that Ne cannot separate for realistic values of the Ne abundance in WDs.

Rates of neutrino energy losses are taken from Itoh et al. (1996), with the exception of plasma neutrino emission, taken from the more accurate Haft, Raffelt & Weiss (1994) calculations.[2] Radiative opacities for temperatures above 10 000 K are taken from Iglesias & Rogers (1996), while below 10 000 K, we employed Saumon & Jacobson (1999) results for pure-H, and Alexander et al. (1997) for pure-He (and the mixed H–He or C–O–He compositions in some tests described in Section 3) compositions.

Electron conduction opacities are from the calculations by Cassisi et al. (2007) in one set of models, and from Blouin et al. (2020) for the H and He envelopes (keeping Cassisi et al. 2007, opacities for the CO cores) in a second set. Blouin et al. (2020) have recently published new, improved calculations of electron conduction opacities for H and He compositions for moderate degeneracy (i.e. when $\theta \sim 1$, where $\theta \equiv T/T_{\rm F}$, and $T_{\rm F}$ is the Fermi temperature) which they have bridged with Cassisi et al. (2007) calculations for strong degeneracy ($\theta \lesssim 0.1$). These new opacities are lower by a factor up to 2.5–3 near the boundary of the temperature-density domain where the new calculations are valid. The treatment of the conductive opacities at the transition from moderate to strong degeneracy is, however, still uncertain – as discussed in detail by Cassisi et al. (2021), see also Blouin et al. (2020) – and is crucial for the envelopes of WD models. Different ways to bridge Blouin et al. (2020) calculations for moderate degeneracy with Cassisi et al. (2007) for strong degeneracy can potentially 'recover' Cassisi et al. (2007) opacities in the regime of H and He WD envelopes, and for this reason, we have calculated models using both sets of opacities for H and He compositions. We will show in Section 4 the main differences between these two sets of models.

Photospheric boundary conditions for $T_{\rm eff}$ below 10 000 K have been obtained from calculations of the non-grey model atmospheres described in S10, while at higher $T_{\rm eff}$, we use the integration of the Eddington grey $T(\tau)$ relation. Superadiabatic convection in the envelope is treated according to the Böhm-Vitense (1958) formalism of the mixing length theory, with mixing length $\alpha_{MLT} = 1.5$ (see Ludwig, Jordan & Steffen 1994). Hydrogen burning through the $p-p$ cycle in the model envelopes is included, using the same reaction rates as in Hidalgo et al. (2018). As discussed later, its effect on our models is negligible.

The bolometric corrections necessary to place our WD cooling tracks in CMDs are based on the results by Bergeron, Wesemael & Beauchamp (1995) and Holberg & Bergeron (2006), the same employed by S10.[3] For each track, we have calculated magnitudes in the Johnson-Cousins, Sloan, Pan-STARSS, *GALEX*, Gaia-DR2, Gaia-eDR3, HST-ACS, HST-WFC3, and *JWST* photometric systems.

To summarize, the main differences with respect to S10 regarding the physics inputs of the models are the inclusion of Ne diffusion, the use of the Blouin & Daligault (2021) CO phase diagram instead of Segretain & Chabrier (1993), and the Cassisi et al. (2007) (and alternatively Blouin et al. 2020) conductive opacities, instead of a combination of the older Hubbard & Lampe (1969) tables and Itoh et al. (1983, 1984) analytic formulae employed by S10.

2.2 Chemical stratification

To determine the initial chemical stratification of WD models of a given mass, we need, in principle, to compute the full evolution of the progenitor, from the main sequence through the challenging thermally pulsing asymptotic giant branch, and post asymptotic giant branch phases (see e.g. Renedo et al. 2010; Camisassa et al. 2016, 2017). It is, however, fair to say that the modelling of these advanced evolutionary stages of low- and intermediate-mass stars is subject to non-negligible uncertainties, mainly related to the efficiency of mass-loss, and internal mixing during the thermal pulses. For example, independent evolutionary calculations show appreciable differences in the relation between the initial mass of the progenitor and the final WD mass (see e.g. Marigo & Girardi 2007; Weiss & Ferguson 2009; Cummings et al. 2018); given that the CO stratification in the WD progeny depends on the initial mass of their progenitors, variations of the initial–final mass relation (IFMR) imply variations of the predicted CO profile for a fixed $M_{\rm WD}$. Also, the mass thickness of the H- and He-rich layers surrounding the CO core depend on how many thermal pulses have been experienced by the progenitor, the timing of the last pulse, and the efficiency of mass-loss during the post asymptotic giant branch phase (see e.g. Althaus et al. 2005, 2015; De Gerónimo et al. 2019), that are still difficult to predict accurately by means of stellar evolution calculations.

Following the philosophy of S10, we provide here calculations with a fixed constant initial thickness of the H and He envelope layers for all WD masses and all initial compositions of the progenitors (see also e.g. Hansen 1999; Fontaine, Brassard & Bergeron 2001; Bédard et al. 2020, for a similar approach), and a fixed, semi-empirical

---

[2] The more recent determination of plasma neutrino emission rates by Kantor & Gusakov (2007) provides results in agreement with Haft et al. (1994), in the temperature-density regime of our calculations.

[3] https://www.astro.umontreal.ca/~bergeron/CoolingModels/

IFMR to determine the core CO stratifications. This choice provides a reference baseline to eventually help disentangle the effect of the existing uncertainties related to core and envelope physical and chemical properties, when comparisons with observations are made.

The H-atmosphere models have ‘thick’ H layers, as in S10; the envelope is made of pure hydrogen layers enclosing a fraction $q(\mathrm{H}) = 10^{-4}$ of the total mass M_{WD}, around pure-He layers of mass $q(\mathrm{He}) = 10^{-2}$, which surround the CO core (the same values chosen by Hansen 1999; Fontaine et al. 2001; Bédard et al. 2020). The He-atmosphere WD models have a pure helium envelope with mass fraction $q(\mathrm{He}) = 10^{-2}$ around the CO core. The chosen orders of magnitude of q(H) and q(He) are informed by results of evolutionary calculations of WD progenitors (see e.g. Iben & MacDonald 1986; Renedo et al. 2010).

With these choices of q(H) and q(He), the surface convection, which eventually develops during the cooling evolution, is not able cross the H–He interface in the H-atmosphere models, or the He–CO interface in the He-atmosphere models. Also, $p-p$ burning slowly changes with time the chemical composition of the deeper parts of the H envelopes of the models, producing a small (in mass) tail of increasing He abundance when moving inwards. However, the cooling times of the models (and the total mass of H and He in the envelope) are not changed appreciably compared to the case of no burning allowed.

Whilst the H and He stratification has been set at the start of the cooling sequence without modelling the previous evolution, the profiles of the C, O, and Ne abundances in the CO cores have been taken from the evolution of models of the chosen progenitors. To this purpose, we have considered the semi-empirical IFMR by Cummings et al. (2018), and for each value of M_{WD} in our model grid, we have derived the corresponding value of the progenitor mass M_{i} from Cummings et al. (2018) formula.[4]

For any given M_{WD}, we have then computed the evolution of the progenitor with mass M_{i} starting from the pre-main sequence, employing the same code and physics inputs of Hidalgo et al. (2018) calculations, including overshooting from the convective cores during the main sequence (but not from the convective envelopes, when present), semiconvection during the core He-burning phase, mass-loss using Reimers (1975) formula with the free parameter η set to 0.3, and an initial solar scaled chemical composition with metal mass fraction $Z = 0.017$ (about solar – see Hidalgo et al. 2018, for details of the code). We are not interested in following the details of the asymptotic giant branch evolution of these models, just in the growth of the He-exhausted core; the initial CO stratification of the WD model has been then taken as the CO abundance profile inside the He-free core of the progenitor, when this has reached a mass equal to M_{WD}.

As an example, the upper panel of Fig. 3 shows the case of the models with $M_{\mathrm{WD}} = 0.77\,\mathrm{M}_{\odot}$; it displays the inner chemical stratification of the progenitor with mass $M_{\mathrm{i}} = 3.1\,\mathrm{M}_{\odot}$ around the time its He-free core has reached $0.77\,\mathrm{M}_{\odot}$. As discussed in Salaris et al. (1997), the chemical profile in the inner region of the He-exhausted core, with constant abundances of C and O, is determined by the maximum extension of the central He-burning convective region. Moving outwards from the centre, the peak in the oxygen abundance (and the corresponding depression of the C abundance) is produced when the He-burning shell crosses the semiconvective region partially enriched in C and O, and ^{12}C is converted into ^{16}O through the $^{12}\mathrm{C}(\alpha,\gamma)^{16}\mathrm{O}$ reaction. Beyond this region, the oxygen profile is built by the He-burning shell moving outwards. Gravitational contraction increases temperature and density in the shell, and given that the ratio between the $^{12}\mathrm{C}(\alpha,\gamma)^{16}\mathrm{O}$ and 3α reaction rates is lower for larger temperatures, the oxygen abundance steadily decreases in the external part of the CO core. The flat abundance profile of Ne is caused by the processing of N in the He core during He-burning through the reactions $^{14}\mathrm{N}\,(\alpha,\gamma)^{18}\mathrm{F}\,(\beta^{+})^{18}\mathrm{O}\,(\alpha,\gamma)^{22}\mathrm{Ne}$; as a result, the final Ne mass fraction is about equal to the initial metal mass fraction Z of the progenitor models.

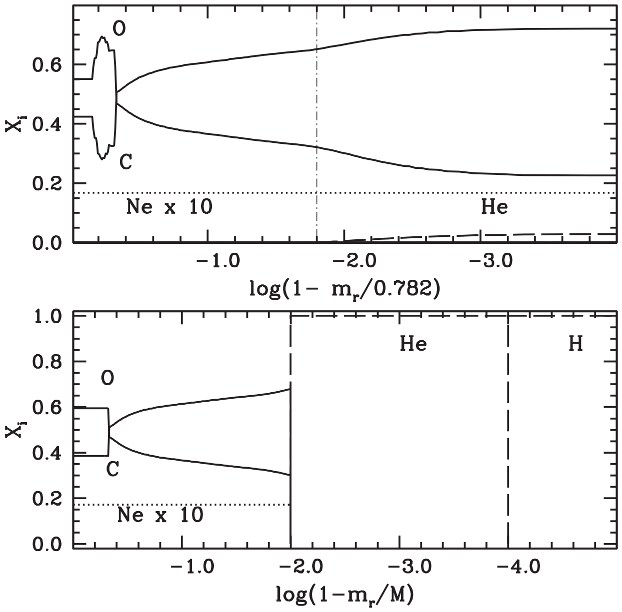

Figure 3. Upper panel: stratification of the C, O, Ne, H, and He abundances in the inner layers of a $3.1\,\mathrm{M}_{\odot}$ asymptotic giant branch model with initial chemical composition about solar. Abundances are given in mass fractions (for the sake of clarity the Ne mass fraction is increased by a factor of 10) and m_r is the mass enclosed within a radial distance r from the centre of the model. The stratification is taken around the time the He-free core (whose boundary is marked by the thin dash–dotted vertical line) has reached $0.77\,\mathrm{M}_{\odot}$, the final WD mass prescribed by the Cummings et al. (2018) IFMR (see text for details). Lower panel: initial chemical stratification adopted for the corresponding $0.77\,\mathrm{M}_{\odot}$ H-atmosphere WD model (M is the total mass of the model).

The lower panel of Fig. 3 shows the chosen initial chemical stratification of the corresponding WD, after the chemical rehomogeneization of the inner core caused by the molecular weight inversion due to the above-mentioned local peak in the O abundance (and dip of the carbon mass fraction) discussed in Salaris et al. (1997).

This kind of chemical profiles is admittedly ‘artificial’, because the CO–He–H chemical transitions are not predicted to be sharp by fully evolutionary calculations (see e.g. Renedo et al. 2010; De Gerónimo et al. 2018, for some examples). This can be seen also in the upper panel of the same figure, which displays the beginning of a slowly rising He abundance from the boundary of the He-free core, with C and O abundances different from zero in a region where He is also present. In Section 3, we will show that imposing these sharp transitions instead of more realistic ones does not have any major effect on the cooling time-scales of the models (but they have an

---

[4] We have considered Cummings et al. (2018) results obtained using the Bressan et al. (2012) models for the WD progenitor lifetimes, instead of the Choi et al. (2016) ones. The differences in the predicted progenitor masses are, however, negligible for M_{WD} lower than $1\,\mathrm{M}_{\odot}$, and reach at most $0.6\,\mathrm{M}_{\odot}$ for $M_{\mathrm{WD}} = 1.1\,\mathrm{M}_{\odot}$.

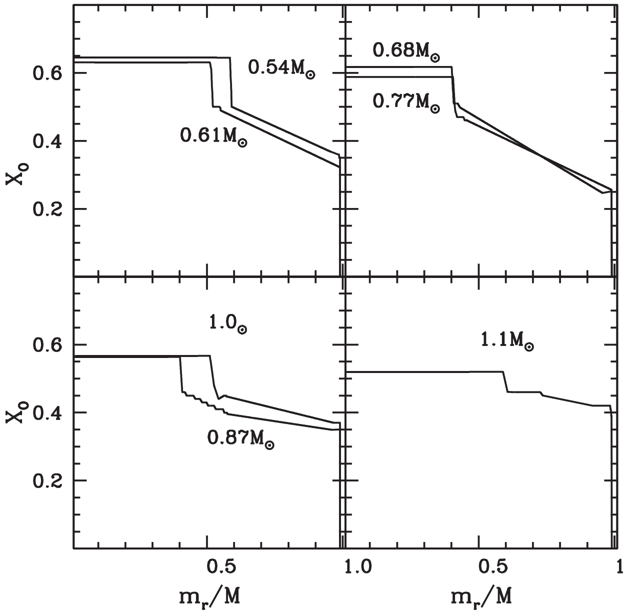

Figure 4. Oxygen abundance (mass fraction) stratification adopted for our models (see text for details).

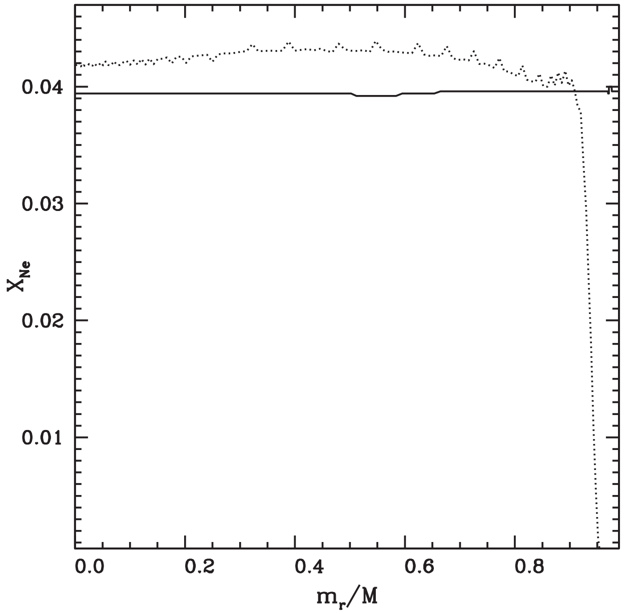

Figure 5. Initial (solid line) and final (dotted line) Ne abundance stratification (abundance in mass fraction) of a 0.61 $M_\odot$ H-atmosphere model from a progenitor with $Z = 0.04$ (see text for details).

impact on the model asteroseismic properties, see e.g. Giammichele et al. 2017).

In this way, we have determined the initial chemical profiles for all selected values of $M_{\rm WD}$, from calculations of progenitor models with $Z = 0.017$. Fig. 4 displays the resulting oxygen stratifications (given in mass fraction $X_{\rm O}$) across the CO cores, with the central value of $X_{\rm O}$ typically decreasing with increasing $M_{\rm WD}$. The corresponding carbon mass fraction $X_{\rm C}$ is given by $X_{\rm C}$ = 1-$X_{\rm O}$-Z, where Z is the progenitor metallicity, which is equal to a very good approximation to the mass fraction of Ne ($X_{\rm Ne}$) across the core.

Given the importance of the amount of Ne in the core for the cooling time-scales of the models (see e.g. García-Berro et al. 2008), for each WD mass, we have calculated models for five different initial Ne flat abundance profiles, corresponding to progenitors' metallicities equal to Z =0.006, 0.01, 0.017, 0.03, 0.04. When the mass fraction of Ne is below 0.006, we found that the effect on both H- and He-atmosphere models' cooling time-scales is always negligible, hence we have also computed an additional set with no Ne, representative of WDs from progenitors with $Z < 0.006$. For all these sets of calculations with varying Ne abundances, we have kept the same CO profiles determined as described before (see Section 3).

Before closing this section, we wish to briefly comment on the results by Giammichele et al. (2018), later refined by Charpinet et al. (2019), who have determined the radial chemical stratification of the ∼0.56 $M_\odot$ pulsating He-atmosphere WD KIC08626021, using asteroseismic techniques.[5] In the helium-free layers, they found the presence of a central homogeneous core with a mass of ∼0.45 $M_\odot$ and $X_{\rm O}$ ∼0.84, and also an external, very thin (in mass) almost pure carbon buffer (see Fig. 3 in Charpinet et al. 2019). As discussed extensively by De Gerónimo et al. (2019), within our current understanding of the evolution of WD progenitors, it is difficult to reproduce the chemical structure of this star as derived from asteroseismology. For example, looking at the oxygen stratification of our 0.54 $M_\odot$ models (a mass very close to the value estimated for KIC08626021) shown in Fig. 4, the central $X_{\rm O}$ is much lower than the asteroseismic value, and the chemically homogeneous inner core has a mass of ∼0.32 $M_\odot$ instead of 0.45 $M_\odot$. We have assessed the impact of this asteroseismic CO profile on our WD models by computing the evolution of 0.54 $M_\odot$ WDs with hydrogen and helium atmospheres, respectively (the thickness of the H and He envelopes is the same adopted in the calculations described in this section) and no Ne – using Cassisi et al. (2007) conductive opacities – employing the CO stratification determined by Charpinet et al. (2019). We have found small differences in the cooling times compared to our calculations with the chemical profile of Fig. 4, amounting at most to 4 per cent (cooling times being shorter with the asteroseismic chemical stratification) at luminosities $\log(L/L_\odot) \sim -4.9$.

2.3 The effect of Ne diffusion

As discussed in detail in the literature (see e.g. Bildsten & Hall 2001; García-Berro et al. 2008), ^{22}Ne nuclei have a larger mass-to-charge ratio than ^{12}C and ^{16}O (the ratio between atomic weight and charge is larger than 2 for ^{22}Ne); this results in a net downward gravitational force on Ne, with a consequent slow diffusion towards the centre in the liquid layers, and the release of gravitational energy that contributes to the WD energy budget.

Fig. 5 displays the initial Ne abundance profile in the CO core of our 0.61 $M_\odot$ H-atmosphere calculations with a $Z = 0.04$ progenitor, and the final Ne stratification when the core has fully crystallized. On the whole, the final distribution of Ne is more concentrated towards the centre compared to the initial one, and the details of the final abundance profile arise from the interplay between the settling of Ne towards the centre, and the inhibition of diffusion at the crystallization front, that moves outwards with time.

As already mentioned, this displacement of Ne towards the centre causes a release of gravitational energy, that slows down the cooling of the models. This is shown by Figs 6 and 7, which display the extra time $\Delta t_{\rm cool}$ that selected H-atmosphere and He-atmosphere models

---

[5] See also the preliminary results by Charpinet et al. (2021) for five more objects.

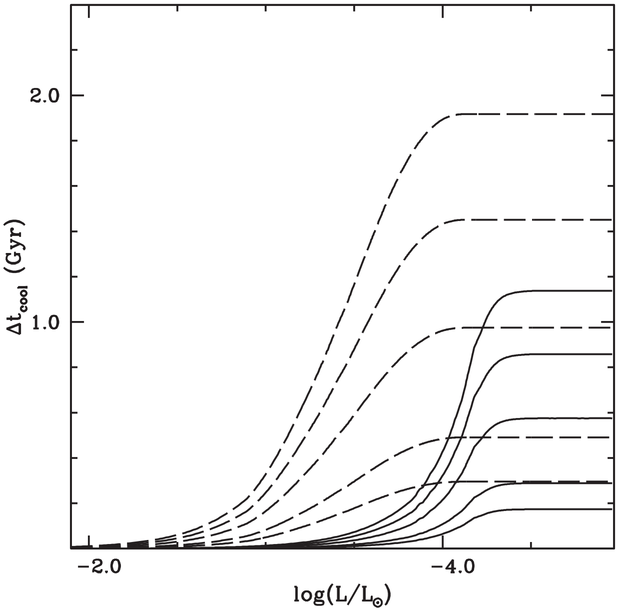

Figure 6. Cooling time delay $\Delta t_{\rm cool}$ (in Gyr) as a function of the luminosity, caused by the diffusion of Ne in 0.61 $M_\odot$ (solid lines) and 1.0 $M_\odot$ (dashed lines) H-atmosphere WD models, from progenitors with Z = 0.006, 0.01, 0.017, 0.03, 0.04 (in order of increasing maximum $\Delta t_{\rm cool}$), respectively.

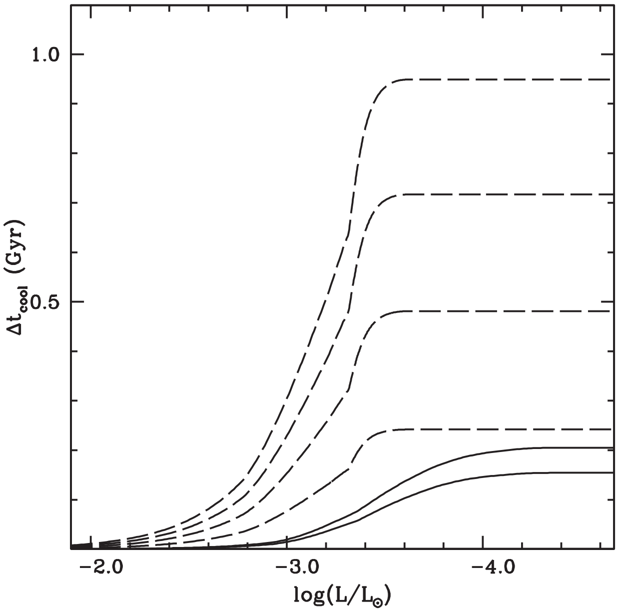

Figure 7. As Fig. 6 but for the corresponding He-atmosphere models. The displayed 0.61 $M_\odot$ calculations are for progenitors with $Z = 0.03$ and 0.04; the 1.0$M_\odot$ calculations are for progenitors with Z = 0.01, 0.017, 0.03, 0.04 (in order of increasing maximum $\Delta t_{\rm cool}$). The cooling delay for models from lower metallicity progenitors are negligible.

– calculated with Cassisi et al. (2007) electron conduction opacities – take to cool down to a given luminosity, due to the diffusion of Ne. In addition to the mass of the model, the progenitor metallicity here plays a major role, because an increase of the amount of Ne in the core increases $\Delta t_{\rm cool}$. These delays can have the same order of magnitude of the effect of latent heat release plus phase separation upon crystallization of the CO mixture (which amounts to ∼1.85 Gyr for the 0.61 $M_\odot$ H-atmosphere models), depending on the initial Ne abundance.

The values of $\Delta t_{\rm cool}$ due to Ne diffusion (and also crystallization) are, in general, smaller for He-atmosphere models, due to the lower opacities of the non-degenerate envelope; and for the lower mass models they are already negligible for progenitors around solar metallicity.

3 TESTS ON THE INITIAL CHEMICAL PROFILES

In the previous section, we have compared the cooling times of WD models from progenitors with different initial metallicities. These models have been computed with Ne abundances appropriate for the progenitor metallicity, but with a fixed CO stratification at a given $M_{\rm WD}$, determined from progenitors with metallicity about solar and mass derived from a single IFMR. In this way, we have quantified the effect of Ne diffusion on the cooling times of our models, for different Ne abundances and $M_{\rm WD}$.

In this section, we want first to assess whether changing just the Ne abundance in the core is a reasonable approximation to determine reliable cooling times for WDs produced by progenitors with varying metallicity. Whilst the Ne mass fraction is always to a very good approximation equal to Z and uniform across the core for any $M_{\rm WD}$, irrespective of the assumed values of $M_{\rm i}$, the situation for CO is more complex. In fact, the CO stratification for a given $M_{\rm WD}$ depends in principle on the progenitor Z through a combination of the effect of Z on the CO profiles at fixed $M_{\rm i}$, and the effect of metallicity on the IFMR, that associates a progenitor mass $M_{\rm i}$ to a given $M_{\rm WD}$.

Semi-empirical determinations of the IFMR are based on objects of metallicity typically around solar, apart from the lowest mass WDs included in Cummings et al. (2018) IFMR adopted here, that come from observations of the globular cluster NGC 6121. Therefore, we do not have empirical indications of how the IFMR globally changes with changing progenitor metallicity, with the consequent not well-established impact on the CO stratification of the WD models.

As already mentioned, theoretical predictions of the IFMR do not provide consistent results. The only qualitative trend on which various theoretical calculations of asymptotic giant branch evolution (see e.g. Marigo & Girardi 2007; Weiss & Ferguson 2009) generally agree is that, with decreasing Z, the value of $M_{\rm i}$ for a fixed $M_{\rm WD}$ tends typically to decrease, at least for $M_{\rm i}$ above ∼2–2.5 $M_\odot$. Assuming this qualitative trend is real, we have performed the following test on H-atmosphere models, calculated with the Cassisi et al. (2007) conductive opacities.

The upper panels of Fig. 8 display pairs of oxygen abundance profiles employed to calculate 0.87 and 1.1 $M_\odot$ models, respectively. We have considered first our reference abundances determined as described in the previous section, which in this case came from progenitors with $M_{\rm i}$ = 3.6 $M_\odot$ (for $M_{\rm WD}$ = 0.87 $M_\odot$), and $M_{\rm i}$ = 6.4 $M_\odot$ (for $M_{\rm WD}$ = 1.1 $M_\odot$), both calculated with $Z = 0.017$. For these progenitor, the mass of the He-free core has increased by, respectively, ∼0.16 and ∼0.18 $M_\odot$ compared to the values at the first thermal pulse.

The second set of oxygen stratifications have been obtained by considering progenitors with $Z = 0.0002$ (a low metallicity typical of metal-poor Galactic globular clusters) and masses $M_{\rm i}$ such that the models reach $M_{\rm WD}$ = 0.87 and 1.1 $M_\odot$ when the mass of their He-free cores had grown by ∼0.16 and ∼0.18 $M_\odot$, respectively, compared to the values at the first thermal pulse, like the case of our reference IFMR. The corresponding values of $M_{\rm i}$ are equal to 2.5 and 5 $M_\odot$, lower than the values prescribed by our reference IFMR, consistent

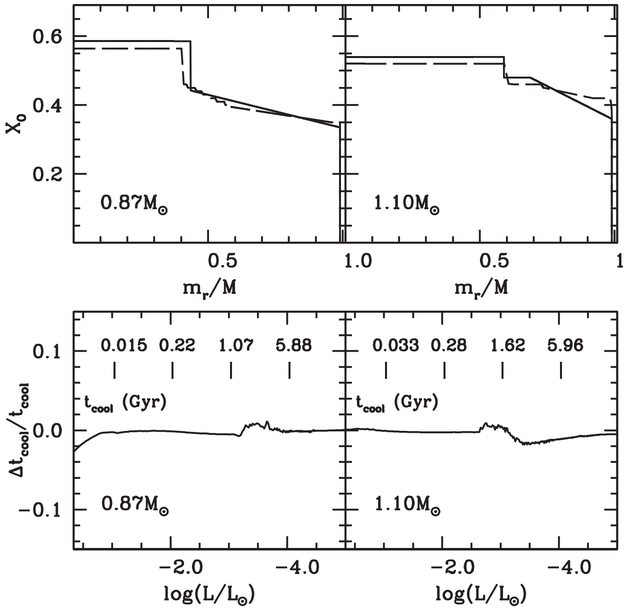

Figure 8. Upper panels: pairs of oxygen abundance profiles (abundance in mass fraction) employed for the calculation of 0.87 and 1.1 $M_\odot$ H-atmosphere WD models. The dashed lines display our adopted reference profiles, whilst the solid lines correspond to the case of metal poor progenitors with $Z = 0.0002$ (see text for details). Lower panels: relative difference between the cooling times obtained using the CO stratification of the metal poor progenitor and those obtained from the reference stratification, as a function of the luminosity. Selected cooling ages from the calculations with the reference profiles are marked.

with the qualitative trend expected from asymptotic giant branch evolutionary models.

For each value of $M_{\rm WD}$, the two abundance profiles from progenitors with different metallicities turn out to be very similar. In the assumption that our assumed metal poor IFMR is the 'real' one, then we can expect that if we use our reference CO stratification to calculate models for WDs in $Z = 0.0002$ populations, we will determine cooling times negligibly different from the case of using the appropriate metal poor IFMR.

This is shown in the lower panels of the same figure, which compare the cooling times of our reference 0.87 and 1.1 $M_\odot$ calculations without Ne (because its effect on the cooling times is negligible at this metallicity) with models calculated using the core stratification from the appropriate $Z = 0.0002$ progenitors (and no Ne). We find almost negligible fractional differences of the cooling times, the largest values being at most equal to 2 per cent.

Given the results of this test – based on necessarily arbitrary assumptions – that somehow mimics the qualitative behaviour of the IFMR with Z as predicted by theoretical asymptotic giant branch models, and the lack of empirical assessments of how the IFMR varies with metallicity, we consider our models calculated with fixed IFMR and CO profiles and varying Ne abundances (see Section 2) to be an acceptable choice to study the cooling of WDs in populations with different metallicities.

3.1 Testing the idealized chemical interfaces

Another assumption – common in the literature – made in our WD model calculations is that the CO–He–H chemical transitions are sharp, with an abrupt switch from the CO (and Ne) core to a pure-He envelope, and from the He envelope to a pure-H envelope. As mentioned in the previous section, this is just an idealization. In reality, progenitor model calculations show a narrow (in mass) transition region around the He-free core, where the He abundance progressively increases outwards, and the C and O abundances drop to zero, due to incomplete burning in the He-shell. Additionally, H and He are not 'separated' in the envelopes of the asymptotic giant branch progenitors, even considering the effect of atomic diffusion during the previous evolution, and pure-H and He envelopes do not account for the metals in the initial chemical composition of the progenitor. The CNO of the original chemical composition can be involved in hydrogen burning if the mass of the hydrogen layers is large enough (see e.g. Althaus et al. 2015 and below).

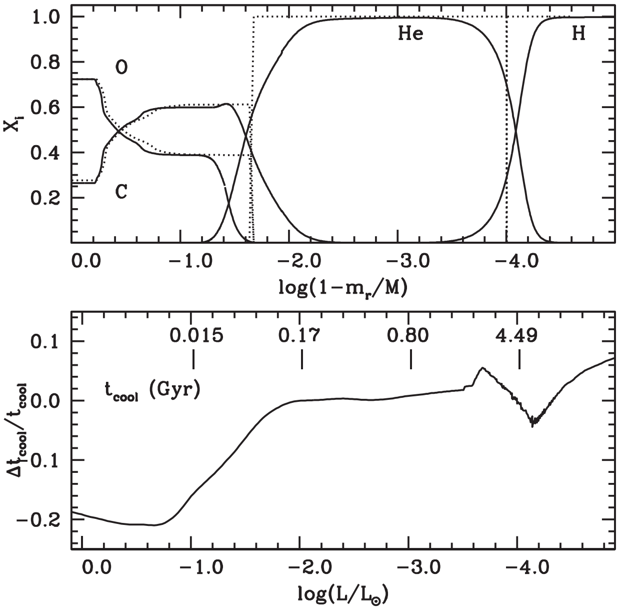

Figure 9. Upper panel: Solid lines display the C, O, He, and H stratification (abundances in mass fraction) at the beginning of the cooling sequence of 0.61 $M_\odot$ H-atmosphere models by Renedo et al. (2010). The dotted lines display our adopted core stratification with CO profile determined as described in Section 2.2, plus stratified pure-H and He envelopes which match the total mass of H and He of Renedo et al. (2010) models. Lower panel: Relative difference of cooling times as a function of luminosity with respect to Renedo et al. (2010) calculations, of 0.61 $M_\odot$ models calculated using the stratification with pure-He and H envelopes shown in the upper panel (dotted line – see text for details). Some reference cooling ages from Renedo et al. (2010) calculations are marked.

As discussed for example in Renedo et al. (2010), atomic diffusion during the WD cooling makes helium and metals sink from the outer envelope, producing a thin (in mass) pure-H layer that thickens as evolution proceeds. Chemical transitions exhibit increasingly less sharp discontinuities, and the metals progressively sink towards deeper and deeper regions of the envelope. Overall, the chemical stratification of WD model envelopes is expected not only to be initially without sharp chemical transitions, but also to change slowly during the cooling. To test the effect of the simplified chemical transitions adopted in our models on the predicted cooling ages, we have performed the following numerical experiment.

We have considered the C, O, He, H chemical stratification of the 0.61 $M_\odot$ H-atmosphere WD model by Renedo et al. (2010), calculated from a progenitor with $M_{\rm i} = 2\,M_\odot$ and metallicity $Z = 0.01$, taken at $\log(L/L_\odot) \sim 1.0$, and displayed in the upper panel of Fig. 9. In this plot, the mass fractions of C and O below 10^{-4} found in the He- and H-rich envelopes of Renedo et al. (2010) model are set to zero; the nitrogen abundance, that is accounted for by Renedo et al. (2010) is also set to zero everywhere. The total masses of hydrogen and helium in the envelope correspond to $q(\mathrm{H}) = 1.3 \times 10^{-4}$ and $q(\mathrm{He}) = 2.3 \times 10^{-2}$, respectively.

Starting from this chemical profiles, we have built the second chemical stratification displayed in the upper panel of Fig. 9, which mimics the way we have built the chemical make-up of our new BASTI models presented in this paper (see Section 2.2). The CO–He–H discontinuities are sharp, the envelope is made of pure-H and pure-He layers with $q(\mathrm{H}) = 1.3 \times 10^{-4}$ and $q(\mathrm{He}) = 2.3 \times 10^{-2}$, to preserve the total amounts of H and He of Renedo et al. (2010) initial model, and the CO stratification has been obtained by taking the CO abundance profile inside the He-free core of Renedo et al. (2010) model. Given that we do not account for the small amount of C and O in the abundance tails that overlap the helium envelope (i.e. in the region between $\log(1 - m_r/M)$ between ~ -1.2 and ~ -2.4), we needed to apply a very small rescaling of the mass coordinate in the CO core, to conserve the total mass of the model. This profile is a proxy for Renedo et al. (2010) initial profile, built essentially like the chemical stratification of the set of new BASTI WD models that we are presenting in this paper.

Using this chemical stratification, we have calculated with our code the evolution of a 0.61-$\mathrm{M}_{\odot}$ WD model using the same EOS, boundary conditions, radiative and conductive opacities, neutrino energy loss rates, and CO phase diagram employed by Renedo et al. (2010), who used the LPCODE for their calculation. For this test – like for all our BASTI WD models – we neglect the evolution of the H and He profiles due to atomic diffusion, set all metal abundances to zero in the non-degenerate envelope, and hence we neglect also the occurrence – a small effect in Renedo et al. (2010) calculations – of CNO burning in the hydrogen envelope.

The lower panel of Fig. 9 displays the relative difference of the cooling times (zeroed at $\log(L/L_{\odot}) \sim 1.0$) with respect to Renedo et al. (2010) models.[6] Our calculation displays systematically shorter ages (up to about 20 per cent shorter) during the early phases of cooling, when the age of the models is of the order of 10 Myr or less. This difference is most likely due to the different thermal structures at $\log(L/L_{\odot}) \sim 1.0$, the start of our calculations.[7] By $\log(L/L_{\odot}) \sim -1.8$ and cooling ages around 100 Myr neutrino emission – by now inefficient – has erased any difference of the initial thermal structure of the models, and the cooling times become almost identical. Differences reach at most about ±6 per cent when $\log(L/L_{\odot})$ goes below ~ -4.0, corresponding to ages above ~ 4.5 Gyr. The radius of our models is systematically lower than Renedo et al. (2010) results, differences amounting to just about 3 per cent at $\log(L/L_{\odot}) = 0.5$, decreasing to 1.5 per cent and $\log(L/L_{\odot}) = -2.0$, and below 1 per cent when $\log(L/L_{\odot})$ is lower than ~ -3.

To summarize, this test shows that the use of sharp chemical interfaces, the neglect of the abundance of the metals in the H- and He-rich layers, and the effect of atomic diffusion, and CNO burning in the envelope of models with total H and He mass fractions similar to the choice adopted in our BASTI calculations, have a minor effect on the models' cooling times and radius, amounting to at most a few per cent.

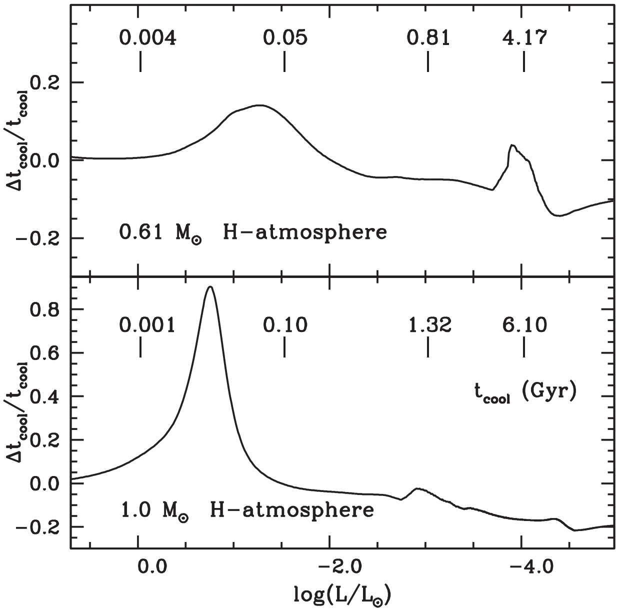

Figure 10. Relative difference of cooling times as a function of luminosity for our 0.61 and 1.0 $\mathrm{M}_{\odot}$ H-atmosphere models with no Ne (corresponding to metal poor populations), calculated with Blouin et al. (2020) and Cassisi et al. (2007) opacities, respectively. A positive difference means that models computed with Blouin et al. (2020) opacities have longer cooling times. Some reference cooling ages from the calculations with Cassisi et al. (2007) opacities are marked.

4 THE ROLE OF THE ELECTRON CONDUCTION OPACITIES

As motivated and as discussed in Section 2.1, we have computed two sets of new BASTI WD calculations, employing the Cassisi et al. (2007) and Blouin et al. (2020) conductive opacities, respectively. Blouin et al. (2020) and Cassisi et al. (2021) have shown that WD models calculated with Blouin et al. (2020) conductive opacities display longer cooling times at bright luminosities and shorter cooling times at faint luminosities, compared to calculations with Cassisi et al. (2007) opacities; Figs 10 and 11 confirm their results, displaying the relative difference of the cooling ages of 0.61 and 1.0 $\mathrm{M}_{\odot}$ H- and He-atmosphere models calculated with both sets of opacities.

The lower Blouin et al. (2020) conductive opacities for the H and He layers induce a faster cooling of the core, which in turns reduces the efficiency of neutrino cooling at bright luminosities, and increases the cooling times at a fixed value of $\log(L/L_{\odot})$. The absolute values of the cooling times at these luminosities are, however, fairly short, well below 100 Myr. With decreasing luminosities, the cooling times calculated with Blouin et al. (2020) opacities become increasingly shorter than calculations with Cassisi et al. (2007) opacities, because of the faster cooling of the structure, and differences increase with increasing M_{WD}. This trend is temporarily broken by the earlier start of CO crystallization in the models with Blouin et al. (2020) opacities, and the associated earlier onset of the release of latent heat and extra energy due to phase separation.

For initial Ne abundances that have an impact on the cooling times of the models, the trends shown in Figs 10 and 11 are unchanged. Due

---

[6] The result of this comparison is significant, given that in Salaris, Althaus & García-Berro (2013), we have shown how WD models calculated with the LPCODE and our BASTI code using the same physics inputs and initial chemical stratification, have cooling times within 2 per cent or better, and radii consistent at the 0.5 per cent level.

[7] Renedo et al. (2010) followed the full evolution from the main sequence to the WD stage of the progenitor, whilst we have converged an initial 'artificial' structure at $\log(L/L_{\odot}) \sim 1.0$, with the chosen total mass and chemical profile.

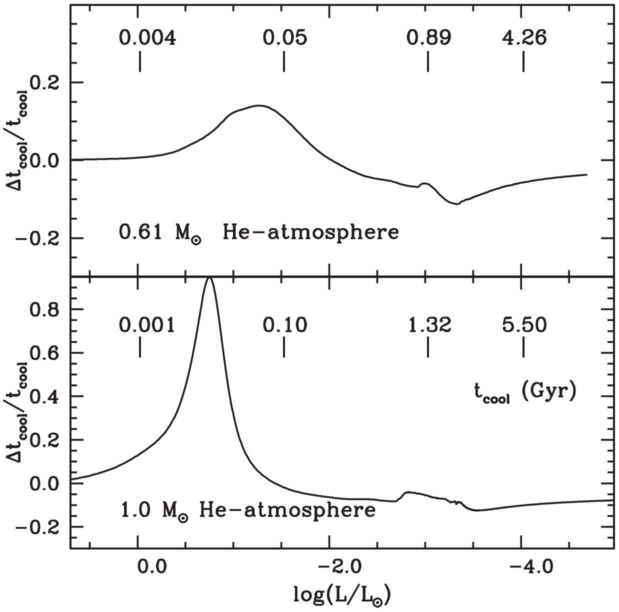

Figure 11. Same as Fig. 10, but for He-atmosphere models.

to the lower opacity of the denser layers of the envelope, the cooling delay caused by the diffusion of Ne in the liquid phase is shorter in models with Blouin et al. (2020) opacities, but the increase of the relative age differences at low luminosities is however small, by at most a few per cent for the higher masses and higher Ne abundances.

5 SEDIMENTATION OF IRON IN THE CORE

After C, O, and Ne, the next more abundant element in the CO core is predicted to be ^{56}Fe (hereafter Fe), part of the initial metal content of the WD progenitors. For the solar scaled metal mixture by Caffau et al. (2011) used in our Hidalgo et al. (2018) progenitor calculations, the mass fraction of Fe is equal to about 8.8 per cent of *Z*.

Caplan et al. (2021) have very recently computed new phase diagrams for a COFe ternary mixture and performed molecular dynamics calculations, showing the Fe present in WD CO cores can precipitate to form an inner iron core during crystallization. This process would release energy (like the diffusion of Ne, or the phase separation of the CO mixture) slowing down the cooling of the models. The sedimentation of Fe was already briefly explored by Segretain & Chabrier (1993) and Segretain et al. (1994), and discussed in more details by Xu & van Horn (1992), making use of calculations of earlier phase diagrams. The details of this process are still uncertain, and various outcomes are possible regarding the chemical stratification of the core during the crystallization of the C, O, and Fe mixture (see Caplan et al. 2021); here, we discuss the more standard scenario presented by Caplan et al. (2021), making a very preliminary estimate of the effect of Fe sedimentation on the cooling times of our models.

When $\Gamma_{\rm C} = 6^{5/3}(2.275\,10^5/T)(\rho/2)^{1/3}$ (with density given in g cm^{-3} and temperature in K – the Coulomb parameter of a pure-C composition) reaches a critical value equal to 140 in a layer of the CO core, its Fe precipitates on very short time-scales towards the centre; we assume here that the fraction of Fe that precipitates is 100 per cent (it could be less than this, according to Caplan et al. 2021) and that this iron settles virtually instantaneously at the centre, replacing C and O (and we assume also Ne, although the fate of Ne is not discussed in the paper by Caplan et al. 2021, and another possibility is that this core containing the precipitated Fe is made instead of a C, O, Fe alloy). As the cooling proceeds, more external layers reach $\Gamma_{\rm C} = 140$, and the mass of this pure-Fe core increases, until the CO mixture starts to crystallize and Fe sedimentation stops (Caplan et al. 2021, speculate that Fe sedimentation might continue also after C and O start to crystallize). From this moment on, the CO crystallization proceeds like in the case of neglecting the presence of Fe.

We have implemented this process to follow the evolution of our $M_{\rm WD} = 0.54\,{\rm M}_\odot$ and $M_{\rm WD} = 1.0\,{\rm M}_\odot$ models, respectively, coming from progenitors with $Z = 0.04$, to maximize the amount of Fe in the core. This metallicity corresponds to an Fe mass fraction $X_{\rm Fe} = 0.0035$. In the calculations, we assumed that the diffusion of Ne continues also during the sedimentation of Fe.

For the $M_{\rm WD} = 0.54\,{\rm M}_\odot$ case, all iron within the inner 11 per cent in mass of the CO core is displaced to form a pure-Fe core with mass $M_{\rm Fe} = 0.00021\,{\rm M}_\odot$, before the CO component starts to crystallize (this happens when $\Gamma_{\rm C} \sim 160$ in the innermost CO layers outside the Fe core). The layers depleted in Fe are within the flat part of the CO abundance stratification, that spans the inner 55–60 per cent in mass of the core (see Fig. 3).

The C, O, and Ne removed from the layers now belonging to the iron core replace the heavier Fe in the layers affected by sedimentation, and this causes a small inversion of the mean molecular weight with the overlying Fe-rich layers. The whole region beyond the iron core that originally had a homogeneous CO stratification gets mixed by convection to cancel this inversion; and a part of the energy gained by the sedimentation of Fe is absorbed in these convective layers.[8] As a result, the C and O abundances in these mixed layers are only very slightly changed, by much less than 1 per cent. The Ne abundance profile, which is affected by diffusion, is rehomogenized in these layers, but the effect on the contribution of the further development of Ne diffusion to the model energy budget is negligible.

The cooling age of the models increases by ∼150 Myr in the range between $\log(L/L_\odot) \sim -3.8$ and -3.9 when we use the Blouin et al. (2020) opacities (at cooling ages around 2.5 Gyr), and by about 190 Myr between $\log(L/L_\odot) \sim -3.9$ and -4.0 in models calculated with Cassisi et al. (2007) opacities (at cooling ages around 3.5 Gyr).

For the $M_{\rm WD} = 1.0$ calculations, the Fe core mass at the end of the sedimentation is equal to $M_{\rm Fe} = 0.00057\,{\rm M}_\odot$, equivalent to about 16 per cent of the total Fe in the CO core; as a result, the cooling age increases by ∼120 Myr in the range between $\log(L/L_\odot) \sim -2.6$ and -2.8 in models calculated with Blouin et al. (2020) opacities (at cooling ages around 790 Myr), and by about 200 Myr between $\log(L/L_\odot) \sim -2.7$ and -2.9 in models calculated with Cassisi et al. (2007) opacities (at cooling ages around 1 Gyr).

6 COMPARISON WITH OTHER MODELS

To put our new calculations in the broader context of existing WD models, we make first a comparison with our previous S10 results. While the models' radii change by less than 1 per cent compared to S10, the same is not true regarding the cooling times. As an example, Figs 12 and 13 compare the cooling times of our 0.61 M$_\odot$ H-atmosphere and He-atmosphere calculations with their S10 counterparts, which do not include Ne diffusion.

---

[8] Also, during the CO crystallization, part of the energy gained is absorbed by the layers that are rehomogenized by the convective episodes caused by phase separation (see e.g. Isern et al. 2000).

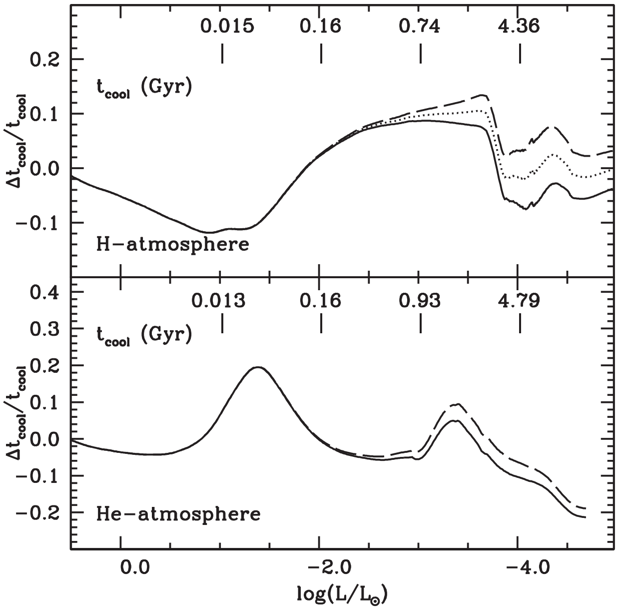

Figure 12. Relative difference of cooling times (in Gyr) as a function of luminosity with respect to the 0.61 M$_\odot$ H-atmosphere calculations from S10 of, respectively, our new 0.61 M$_\odot$ H-atmosphere calculations with Cassisi et al. (2007) opacities without Ne diffusion (solid line), with Ne diffusion and $Z = 0.017$ Ne abundance (dotted line), with Ne diffusion and $Z = 0.04$ Ne abundance (dashed line). Some reference ages from S10 calculations are marked.

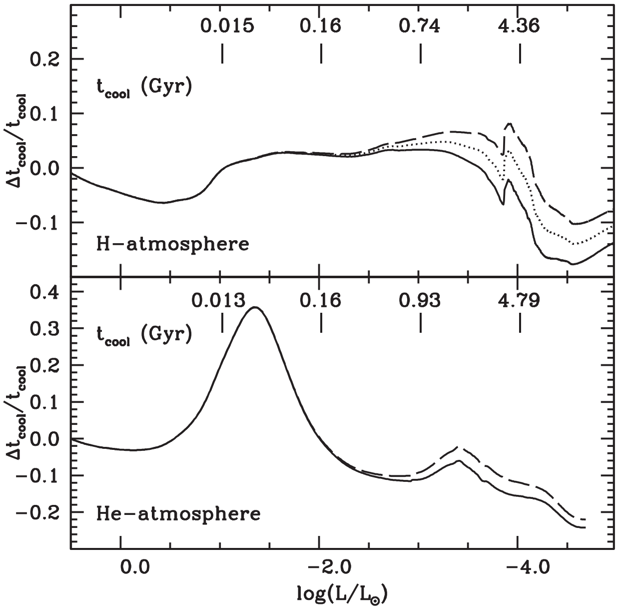

Figure 13. As Fig. 12, but for our new models calculated with Blouin et al. (2020) opacities.

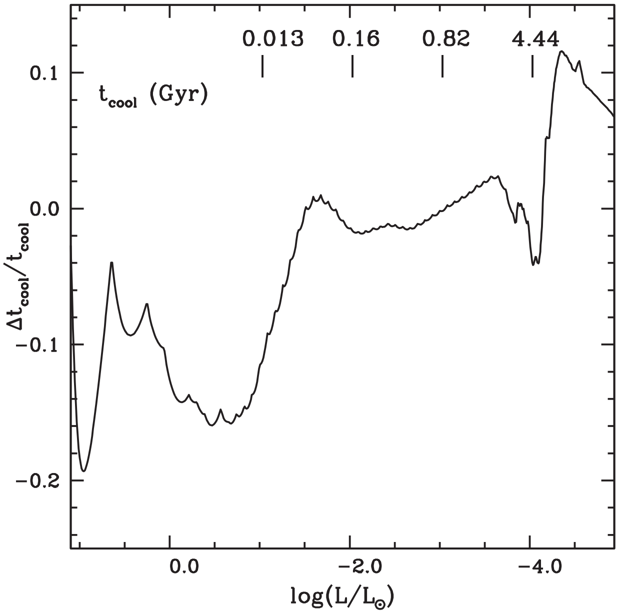

Figure 14. Relative difference of the cooling times (zeroed at $\log(L/L_\odot) = 1.1$) as a function of luminosity between our 0.61 M$_\odot$ H-atmosphere cooling track with Ne abundance from a $Z = 0.017$ progenitor, and a 0.6 M$_\odot$ H-atmosphere track with solar metallicity progenitor from Camisassa et al. (2016). Some reference cooling ages from Camisassa et al. (2016) calculations are marked.

For $\log(L/L_\odot)$ larger than about ~ -3.5, the ±10 per cent differences of cooling times with our models without Ne diffusion are due just to the older conductive opacities adopted by S10. Below this luminosity, we see the effect also of the new CO phase diagram employed here. The Blouin & Daligault (2021) diagram delays the onset of crystallization compared to the Segretain & Chabrier (1993) diagram used by S10, and the amount of matter redistributed by phase separation for a given $M_{\rm WD}$ is sizably smaller when the Blouin & Daligault (2021) phase diagram is employed. This causes a smaller amount of energy released by CO phase separation, causing a faster cooling compared to S10 models.[9] The CO stratification is also not the same as in S10, although differences are small, and the impact on the crystallization process is relatively minor. When we include Ne diffusion the cooling times increase and eventually, in models calculated with Cassisi et al. (2007) opacities and for supersolar Ne abundances, they become longer than S10 results when $\log(L/L_\odot)$ is below ~ -4. In case of the He-atmosphere models, for both choices of conductive opacities – even when including Ne diffusion – the cooling times of our models at $\log(L/L_\odot)$ below ~ -4 are always shorter than S10 results.

In Fig. 14, we compare the cooling times of our 0.61 M$_\odot$ H-atmosphere models including Ne diffusion and a progenitor metallicity $Z = 0.017$, calculated with Cassisi et al. (2007) opacities, with results by Camisassa et al. (2016) for a 0.6 M$_\odot$ H-atmosphere WD computed with the same conductive opacities, which include Ne diffusion and account for the full evolution of a solar metallicity progenitor.[10] Camisassa et al. (2016) models have a different thickness of the envelope layers compared to our calculations, a different CO stratification and there are some differences in the physics inputs, but we take the results of the comparison of cooling times at face value.

At luminosities above $\log(L/L_\odot)$ ~ -1.5 and ages below ~100 Myr, our models display systematically lower cooling ages,

---

[9] The differences with S10 results due to the use of Blouin & Daligault (2021) phase diagram instead of the Segretain & Chabrier (1993) one are very similar to the results discussed by Althaus et al. (2012). These authors compared models calculated with Segretain & Chabrier (1993) phase diagram and the Horowitz, Schneider & Berry (2010) one, which is very similar to the more recent Blouin & Daligault (2021) diagram.

[10] At http://evolgroup.fcaglp.unlp.edu.ar/TRACKS/newtables.html

most likely due to differences in the thermal structure at the beginning of the cooling evolution. Cooling times are then within ±2–4 per cent down to $\log(L/L_{\odot}) \sim -4$, beyond which our models evolve at a slower speed and display cooling times up to about 10 per cent longer.

7 SUMMARY

We have extended our updated BASTI stellar evolution archive with the inclusion of new models for H- and He-atmosphere CO-core WDs, computed using the C,O, and Ne stratification obtained from new progenitor calculations, adopting a semi-empirical IFMR. We have also updated the model physics inputs compared to the previous S10 BASTI WD models; in particular, we now include Ne diffusion in the core, an updated CO phase diagram, and updated electron conduction opacities.

We have calculated the evolution of models with masses $M_{\rm WD}$ equal to 0.54, 0.61, 0.68, 0.77, 0.87, 1.0, and 1.1 $\mathrm{M}_{\odot}$, made of a CO core surrounded by pure-He layers of mass fraction $q(\mathrm{H}) = 10^{-2}$, and (for H-atmosphere models) outermost H layers enclosing a mass fraction $q(\mathrm{H}) = 10^{-4}$. For any given $M_{\rm WD}$, we have computed the evolution of models with several Ne abundances, appropriate for initial metallicities of the progenitors equal to $Z = 0.006$, 0.01, 0.017, 0.03, and 0.04, corresponding to [Fe/H] = −0.40, −0.20, 0.06, 0.30, and 0.45. We have also models calculated with no Ne, representative of WDs from progenitors with [Fe/H] lower than −0.40 ($Z = 0.006$), because the corresponding small quantities of Ne have a negligible effect on the cooling times of the models. In all these calculations, we have kept fixed the CO abundance profiles to those obtained from progenitors with Z=0.017 ([Fe/H] = 0.06), and the IFMR is kept also unchanged in all calculations, for it is not yet established empirically if/how the IFMR varies as a function of the progenitor metallicity. We estimated that the effect of this assumption on the model cooling times is potentially negligible, when we take into account the qualitative trend with metallicity of the IFMRs predicted by theoretical asymptotic giant branch models.

All our models comprise a CO (and Ne) core surrounded by pure-He and H (in H-atmosphere models) envelopes. These sharp chemical transitions and envelopes made of pure-He and H are actually a simplified description of the chemical structure of a WD. We have performed test calculations which have quantified to at most ±6 per cent the effect on the model cooling times of our idealization of the chemical transitions, and the neglect of the metals in the H and He envelopes.

We have also made a first, preliminary estimate of the effect of Fe sedimentation on the cooling times of WD models, following the recent results by Caplan et al. (2021) regarding the phase diagram of C, O, and Fe mixtures. The effect turns out to be generally minor, but there are still substantial uncertainties on the details of this process.

Two complete sets of calculations have been performed, for two different choices of the electron conduction opacities, to reflect the current uncertainty in the evaluation of the electron thermal conductivity in the crucial (for the H and He envelopes) transition regime between moderate and strong degeneracy. Models calculated with different opacities indeed display non-negligible differences in their cooling times, larger for higher values of $M_{\rm WD}$. In the next paper, we will employ both sets of calculations to study WDs in old stellar populations, with the aim of setting some stringent constraints on how to bridge calculations of conductive opacities for moderate and strong degeneracy, as suggested by Cassisi et al. (2021).

We make publicly available the cooling tracks from both sets of calculations, including cooling times and magnitudes in the Johnson-Cousins, Sloan, Pan-STARSS, *GALEX*, Gaia-DR2, Gaia-eDR3, HST-ACS, HST-WFC3, and *JWST* photometric systems.

ACKNOWLEDGEMENTS

We thank the referee for constructive comments that helped us improving the manuscript. SC acknowledges support from Premiale INAF MITiC, from INFN (Iniziativa specifica TAsP), and from PLATO ASI-INAF agreement no. 2015-019-R.1-2018. MS acknowledges support from STFC Consolidated Grant ST/V00087X/1.

SC warmly thanks the Instituto de Astrofisica de Canarias for the hospitality and the Programa de investigadores visitante de la Fundacion Jesus Serra

DATA AVAILABILITY

All WD tracks in several photometric systems are available at the new official BASTI website http://basti-iac.oa-abruzzo.inaf.it.

REFERENCES

Alexander D. R., Brocato E., Cassisi S., Castellani V., Ciacio F., degl'Innocenti S., 1997, A&A, 317, 90
Althaus L. G., Miller Bertolami M. M., Córsico A. H., García-Berro E., Gil-Pons P., 2005, A&A, 440, L1
Althaus L. G., García-Berro E., Renedo I., Isern J., Córsico A. H., Rohrmann R. D., 2010, ApJ, 719, 612
Althaus L. G., García-Berro E., Isern J., Córsico A. H., Miller Bertolami M. M., 2012, A&A, 537, A33
Althaus L. G., Camisassa M. E., Miller Bertolami M. M., Córsico A. H., García-Berro E., 2015, A&A, 576, A9
Bédard A., Bergeron P., Brassard P., Fontaine G., 2020, ApJ, 901, 93
Bedin L. R., King I. R., Anderson J., Piotto G., Salaris M., Cassisi S., Serenelli A., 2008, ApJ, 678, 1279
Bedin L. R., Salaris M., Piotto G., Anderson J., King I. R., Cassisi S., 2009, ApJ, 697, 965
Bedin L. R., Salaris M., King I. R., Piotto G., Anderson J., Cassisi S., 2010, ApJ, 708, L32
Bedin L. R., Salaris M., Anderson J., Cassisi S., Milone A. P., Piotto G., King I. R., Bergeron P., 2015, MNRAS, 448, 1779
Bedin L. R. et al., 2019, MNRAS, 488, 3857
Bellini A. et al., 2010, A&A, 513, A50
Benvenuto O. G., García-Berro E., Isern J., 2004, Phys. Rev. D, 69, 082002
Bergeron P., Wesemael F., Beauchamp A., 1995, PASP, 107, 1047
Bertone G., Fairbairn M., 2008, Phys. Rev. D, 77, 043515
Bildsten L., Hall D. M., 2001, ApJ, 549, L219
Blouin S., Daligault J., 2021, Phys. Rev. E, 103, 043204
Blouin S., Shaffer N. R., Saumon D., Starrett C. E., 2020, ApJ, 899, 46
Blouin S., Daligault J., Saumon D., 2021, ApJ, 911, L5
Böhm-Vitense E., 1958, ZAp, 46, 108
Bravo E., Isern J., Canal R., Labay J., 1992, A&A, 257, 534
Bressan A., Marigo P., Girardi L., Salasnich B., Dal Cero C., Rubele S., Nanni A., 2012, MNRAS, 427, 127
Caffau E., Ludwig H. G., Steffen M., Freytag B., Bonifacio P., 2011, Sol. Phys., 268, 255
Camisassa M. E., Althaus L. G., Córsico A. H., Vinyoles N., Serenelli A. M., Isern J., Miller Bertolami M. M., García–Berro E., 2016, ApJ, 823, 158
Camisassa M. E., Althaus L. G., Rohrmann R. D., García-Berro E., Torres S., Córsico A. H., Wachlin F. C., 2017, ApJ, 839, 11
Caplan M. E., Horowitz C. J., Cumming A., 2020, ApJ, 902, L44
Caplan M. E., Freeman I. F., Horowitz C. J., Cumming A., Bellinger E. P., 2021, ApJ, 919, 6
Cassisi S., Potekhin A. Y., Pietrinferni A., Catelan M., Salaris M., 2007, ApJ, 661, 1094
Cassisi S., Potekhin A. Y., Salaris M., Pietrinferni A., 2021, A&A, 654, 9
Chabrier G., Mazevet S., Soubiran F., 2019, ApJ, 872, 51

Charpinet S., Brassard P., Giammichele N., Fontaine G., 2019, A&A, 628, L2

Charpinet S., Giammichele N., Brassard P., Fontaine G., Bergeron P., Zong W., Van Grootel V., Baran A. S., 2021, in Castanheira C., ed., Proceedings of the 21st European Workshop on White Dwarfs, preprint (arXiv:2107.03797)

Choi J., Dotter A., Conroy C., Cantiello M., Paxton B., Johnson B. D., 2016, ApJ, 823, 102

Córsico A. H., Benvenuto O. G., Althaus L. G., Isern J., García-Berro E., 2001, New A, 6, 197

Cummings J. D., Kalirai J. S., Tremblay P. E., Ramirez-Ruiz E., Choi J., 2018, ApJ, 866, 21

De Gerónimo F. C., Althaus L. G., Córsico A. H., Romero A. D., Kepler S. O., 2018, A&A, 613, A46

De Gerónimo F. C., Battich T., Miller Bertolami M. M., Althaus L. G., Córsico A. H., 2019, A&A, 630, A100

Deloye C. J., Bildsten L., 2002, ApJ, 580, 1077

Fontaine G., Brassard P., Bergeron P., 2001, PASP, 113, 409

Freese K., 1984, ApJ, 286, 216

Garcia-Berro E., Hernanz M., Isern J., Mochkovitch R., 1988, Nature, 333, 642

Garcia-Berro E., Hernanz M., Isern J., Mochkovitch R., 1995, MNRAS, 277, 801

García-Berro E., Althaus L. G., Córsico A. H., Isern J., 2008, ApJ, 677, 473

García-Berro E. et al., 2010, Nature, 465, 194

García-Berro E., Lorén-Aguilar P., Torres S., Althaus L. G., Isern J., 2011, J. Cosmol. Astropart. Phys., 5, 21

Giammichele N. et al., 2018, Nature, 554, 73

Giammichele N., Charpinet S., Brassard P., Fontaine G., 2017, A&A, 598, A109

Goldsbury R. et al., 2012, ApJ, 760, 78

Haft M., Raffelt G., Weiss A., 1994, ApJ, 425, 222

Hansen B. M. S., 1998, Nature, 394, 860

Hansen B. M. S., 1999, ApJ, 520, 680

Hansen B. M. S. et al., 2004, ApJS, 155, 551

Hansen B. M. S. et al., 2007, ApJ, 671, 380

Hidalgo S. L. et al., 2018, ApJ, 856, 125

Holberg J. B., Bergeron P., 2006, AJ, 132, 1221

Horowitz C. J., Schneider A. S., Berry D. K., 2010, Phys. Rev. Lett., 104, 231101

Hubbard W. B., Lampe M., 1969, ApJS, 18, 297

Hughto J., Schneider A. S., Horowitz C. J., Berry D. K., 2010, Phys. Rev. E, 82, 066401

Iben I. J., MacDonald J., 1986, ApJ, 301, 164

Iglesias C. A., Rogers F. J., 1996, ApJ, 464, 943

Isern J., Hernanz M., Garcia-Berro E., 1992, ApJ, 392, L23

Isern J., García-Berro E., Hernanz M., Chabrier G., 2000, ApJ, 528, 397

Isern J., García-Berro E., Torres S., Cojocaru R., Catalán S., 2018, MNRAS, 478, 2569

Itoh N., Mitake S., Iyetomi H., Ichimaru S., 1983, ApJ, 273, 774

Itoh N., Kohyama Y., Matsumoto N., Seki M., 1984, ApJ, 285, 758

Itoh N., Hayashi H., Nishikawa A., Kohyama Y., 1996, ApJS, 102, 411

Kantor E. M., Gusakov M. E., 2007, MNRAS, 381, 1702

Kilic M., Munn J. A., Harris H. C., von Hippel T., Liebert J. W., Williams K. A., Jeffery E., DeGennaro S., 2017, ApJ, 837, 162

Ludwig H. G., Jordan S., Steffen M., 1994, A&A, 284, 105

Marigo P., Girardi L., 2007, A&A, 469, 239

Mochkovitch R., 1983, A&A, 122, 212

Oswalt T. D., Smith J. A., Wood M. A., Hintzen P., 1996, Nature, 382, 692

Pietrinferni A. et al., 2021, ApJ, 908, 102

Reimers D., 1975, Mem. Soc. R. Sci. Liege, 8, 369

Renedo I., Althaus L. G., Miller Bertolami M. M., Romero A. D., Córsico A. H., Rohrmann R. D., García-Berro E., 2010, ApJ, 717, 183

Richer H. B., Fahlman G. G., Rosvick J., Ibata R., 1998, ApJ, 504, L91

Salaris M., Domínguez I., García-Berro E., Hernanz M., Isern J., Mochkovitch R., 1997, ApJ, 486, 413

Salaris M., García-Berro E., Hernanz M., Isern J., Saumon D., 2000, ApJ, 544, 1036

Salaris M., Cassisi S., Pietrinferni A., Kowalski P. M., Isern J., 2010, ApJ, 716, 1241

Salaris M., Althaus L. G., García-Berro E., 2013, A&A, 555, A96

Saumon D., Jacobson S. B., 1999, ApJ, 511, L107

Saumon D., Chabrier G., van Horn H. M., 1995, ApJS, 99, 713

Segretain L., Chabrier G., 1993, A&A, 271, L13

Segretain L., Chabrier G., Hernanz M., Garcia-Berro E., Isern J., Mochkovitch R., 1994, ApJ, 434, 641

Stevenson D. J., 1980, J. Phys., 41, C2

Straniero O., 1988, A&AS, 76, 157

Tononi J., Torres S., García-Berro E., Camisassa M. E., Althaus L. G., Rebassa-Mansergas A., 2019, A&A, 628, A52

Torres S., García-Berro E., 2016, A&A, 588, A35

von Hippel T., 2005, ApJ, 622, 565

Weiss A., Ferguson J. W., 2009, A&A, 508, 1343

Winget D. E., Hansen C. J., Liebert J., van Horn H. M., Fontaine G., Nather R. E., Kepler S. O., Lamb D. Q., 1987, ApJ, 315, L77

Winget D. E., Sullivan D. J., Metcalfe T. S., Kawaler S. D., Montgomery M. H., 2004, ApJ, 602, L109

Winget D. E., Kepler S. O., Campos F., Montgomery M. H., Girardi L., Bergeron P., Williams K., 2009, ApJ, 693, L6

Xu Z. W., van Horn H. M., 1992, ApJ, 387, 662

This paper has been typeset from a TEX/LATEX file prepared by the author.